Journal of Alloys and Compounds 509 (2011) 1378–1383

Contents lists available at ScienceDirect

Journal of Alloys and Compounds

journal homepage: www.elsevier.com/locate/jallcom

The growth of carbon coating layers on iron particles and the effect of alloying the iron with silicon

Hisato Tokoro [a,*], Shigeo Fujii [b], Yasuhiro Kobayashi [c], Shunsuke Muto [d]

[a] Materials Development Laboratory, New Business Development center, Hitachi Metals Ltd., 2-15-17, Egawa, Shimamoto, Mishima, Osaka 618-0013, Japan
[b] New Business Development center, Hitachi Metals Ltd., 1-2-1, Sibaura, Minato, Tokyo 105-8614, Japan
[c] Research Reactor Institute, Kyoto University Kumatori, Osaka 590-0494, Japan
[d] Department of Materials, Physics and Energy Engineering, Graduate School of Engineering, Nagoya University Furo-cho, Chikusa-ku, Nagoya 464-8603, Japan

ARTICLE INFO

Article history:
Received 24 July 2010
Received in revised form 19 October 2010
Accepted 22 October 2010
Available online 4 November 2010

Keywords:
Coating materials
Iron particle
Carbon coating
Solid phase reduction
Precipitation

ABSTRACT

Magnetic fine particles of metallic Fe coated with graphitic carbon layers were synthesized by annealing Fe_2O_3 particles with carbon powders at 1673 K in nitrogen atmosphere. For comparison, SiC was added to Fe_2O_3. X-ray diffraction measurement showed that the lattice constants of Fe changed depending on the Si contents. Mössbauer spectroscopy confirmed that Fe–Si alloys were formed by the Si addition and that the iron carbide disappeared. Electron microscope images revealed that the thickness of carbon coating layers increased from 24 nm to 36 nm as a result of the Si addition. Soaking tests showed that the corrosion resistance of the carbon-coated Fe particles was improved by the addition of Si. The results suggest that Si caused C to leave the Fe cores and move to the surface to form a carbon coating.

1. Introduction

Magnetic fine particles are used in a wide range of applications such as ferrofluids [1], magnetic recording media [2], magnetic toner [3], magnetooptic devices [4], and biomedical applications [5–8]. Iron oxide (γ-Fe_2O_3, Fe_3O_4) particles are typically used in these applications because of their chemical stability. On the other hand, magnetic metal particles, such as Fe, Co, and Fe–Co alloys, have higher magnetizations than iron oxides. Magnetic metal particles can thus be expected to show improved performance in the applications because they can respond more sensitively to magnetic fields. However, metal particles corrode easily, resulting in the deterioration of their high magnetization property.

To counter the corrosion problem of metal particles, carbon (C) coatings have been investigated. Metallic Co particles with C coatings were synthesized by the ion beam sputtering method [9]. The laser irradiation method was employed to coat Fe particles with C [10]. The C-encapsulated Fe particles were synthesized by arc discharge methods [11,12]. We have also developed an adequate method for mass-production so as to fabricate Fe fine particles encapsulated by C layers through the carbothermic reduction of iron oxide powders [13]. All these metallic particles were successfully coated, however, the mechanism of the coating was not studied in detail.

Saito et al. suggested that the C layers on Fe particles grow following the "dissolution and precipitation" mechanism [11]. At first, C dissolves in liquid Fe at an elevated temperature by an arc discharge. Subsequently, graphitic C layers precipitate on the surface of Fe particles in the cooling process, because the solid solubility limit of C to Fe decrease extremely by 1000 K or less. It is similar to the growth of C nanotubes that uses metallic Fe particles as catalysts [14,15]. Carbon forms a solid solution with Fe, when it reaches the saturation point, and grows to form C nanotubes. The dissolution and precipitation of C is an important mechanism to grow C coating layers on the Fe particles.

In this study, silicon (Si) is added in the carbothermic reduction process so as to examine whether the C coating layers is formed by the precipitation of C from Fe cores. The Si is known to show susceptibility toward graphitization in Fe–C–Si [16]. Here, we investigate the effect of Si on the growth of the C coating layers, and the growth mechanism is discussed.

2. Materials and methods

Iron oxide (α-Fe_2O_3), silicon carbide (SiC), and carbon black (C.B.) powders were used as the starting materials. Their diameters were 0.03, 0.01, and 0.02 μm, respectively. The samples were prepared by mixing the starting materials at a predetermined ratio, followed by annealing at 1673 K for 2 h in nitrogen atmosphere. The mixture ratios are shown in Table 1.

* Corresponding author. Fax: +81 75 961 3167.
E-mail address: hisato_tokoro@hitachi-metals.co.jp (H. Tokoro).

0925-8388/$ – see front matter © 2010 Elsevier B.V. All rights reserved.
doi:10.1016/j.jallcom.2010.10.124

Table 1
Mixture ratio of raw materials, saturation magnetization (*Ms*), and coercivity (*Hc*) of samples.

No.	Si (mass%)	Starting materials (mass%)			*Ms* (Am²/kg)	*Hc* (kA/m)
		Fe_2O_3	SiC	C.B.		
S0	0	75.0	0	25.0	147	2.5
SI	1	74.2	0.76	25.0	152	1.2
S2	2	73.5	1.50	25.0	158	1.1
S3	3	72.7	2.26	25.0	164	0.8
S4	4	72.0	3.00	25.0	159	0.7

Magnetic properties were measured by using a vibrating sample magnetometer (VSM) at room temperature under a field of 1.6 MA/m. X-ray diffraction (XRD) measurements were carried out using a powder diffractometer (PANalytical, model X'pert Pro) to determine metallurgical phases and to estimate lattice constants. It used Cu Kα radiation under an applied power of 45 kV and 40 mA in 2θ angular intervals of 30°–120°. The samples consisted of fcc γ-Fe and bcc α-Fe phases. The volume fraction of γ-Fe phase was obtained by the direct comparison method, using the following equations [17],

$$\frac{I_\gamma}{I_\alpha} = \frac{R_\gamma C_\gamma}{R_\alpha C_\alpha} \quad (1)$$

$$R_{\alpha,\gamma} = \left(\frac{1}{v^2}\right)\left[|F|^2 p\left(\frac{1+\cos^2 2\theta}{\sin^2\theta\cos\theta}\right)\right] e^{-2M} \quad (2)$$

$$C_\alpha + C_\gamma = 1 \quad (3)$$

where $I_{\alpha,\gamma}$ is the peak strength of each phase, $C_{\alpha,\gamma}$ is the volume fraction of each phase, v is the unit cell volume of each phase, F is the structure factor, p is the multiplicity factor, θ is the reflection angle of the peak analyzed, and e^{-2M} is the Debye–Waller factor. The diffraction peaks corresponding to the planes of each phase were compared amongst each other, and then the average value of C_γ in each sample was calculated. The analyzed peaks were as follows: $(1\,1\,0)_\alpha$, $(2\,0\,0)_\alpha$, $(2\,1\,1)_\alpha$, $(1\,1\,1)_\gamma$, $(2\,0\,0)_\gamma$, and $(2\,2\,0)_\gamma$. A Mössbauer spectroscope with a ^{57}Co source was employed by using a conventional constant-acceleration method at room temperature in order to investigate the magnetic structures of the samples. On the Mössbauer measurement, the zero velocity is determined into the center of the spectrum of α-Fe. The microstructure of the samples was observed by using a transmission electron microscope (TEM) under an acceleration voltage of 200 kV. A scanning electron microscope (SEM) was used to observe the surface coating of the samples. The corrosion resistance of the samples was examined by a soaking test, in which the sample of 25 mg was soaked in a 1 ml phosphate buffered saline (PBS) for seven days at room temperature. After the magnetic separation of the samples and the solutions, the iron ion concentration in the solutions was analyzed at different soaking time by using an inductively coupled plasma (ICP) atomic emission spectrometer. In order to estimate the oxidation resistance of the samples, thermogravimetry measurement was conducted. The rate of temperature rise was set at 10 K/min and the samples were heated in air from room temperature to 1273 K. Gibbs free energies (ΔG) for each reaction were calculated using the software HSC Chemistry® 6.0 (Outokumpu technology) to compare the stability of compounds, Fe_3C, SiC, FeSi, and Fe_3Si.

3. Results and discussion

3.1. Magnetic properties depending on Si contents

The magnetic properties of the samples that added 0–4 mass% of Si were listed in Table 1. The addition of Si results in an increase in saturation magnetization (*Ms*) and decrease in coercivities (*Hc*). The dependence of the magnetic properties suggests that Fe–Si alloys would be formed by the addition of SiC particles to the starting materials. The coercivities of Fe–1, 2, 3 wt%Si alloy were reported to decrease with Si contents [18].

3.2. Study of phases by X-ray diffraction measurement

The X-ray diffraction patterns of the samples S0–S4 were measured, and two phases of bcc (α-Fe) and fcc (γ-Fe) were detected. Each lattice parameter was obtained from the X-ray diffraction peaks (Fig. 1). The lattice parameters of bcc and fcc phase become small with the Si additions. The reported lattice parameters of bcc Fe–Si alloys [19], which are single crystals, are plotted in Fig. 1. It is clear that the lattice parameters (a_{bcc}) in the present study almost correspond to the reported ones. This suggests that bcc Fe–Si alloys are successfully formed according to the added composition of Si.

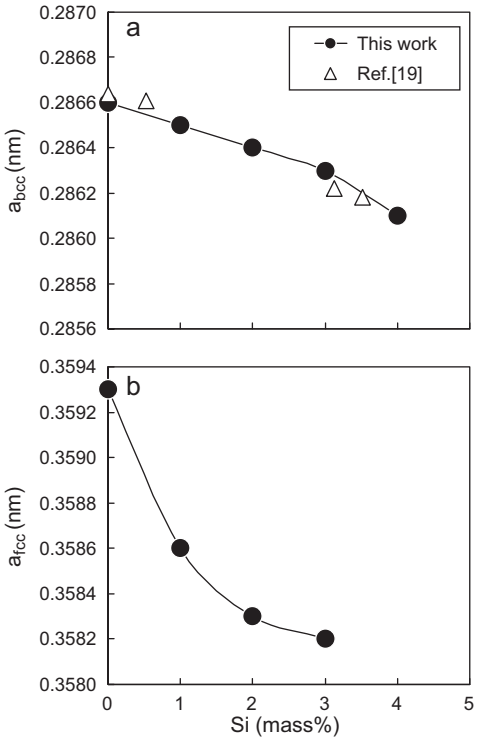

Fig. 1. Lattice constants of (a) bcc-Fe phases, and (b) fcc-Fe phases as a function of Si addition.

The lattice parameters (a_{fcc}) of the fcc phase decrease with the addition of Si. This would be concerning the formation of the fcc Fe–Si alloys.

The peak strength of the fcc phase decreases with the Si additions (Fig. 2(a)). The volume fractions of the fcc phase were estimated by the direct comparison method, using Eqs. (1)–(3) (see section 2). The results are represented by white circles in Fig. 2(b). The volume fractions of the fcc phase were also estimated from Mössbauer spectrum (Fig. 3, Table 2), which are represented by black circles in Fig. 2(b). The fcc phase decreases with the addition of Si, and disappear at 4 mass% of Si. The Fe–Si phase diagram shows that the fcc γ phase of Fe–Si exist in the Si density from 0 mass% to 3.8 mass% at 1185–1587 K [20]. Considering that the annealing temperature was 1673 K, the γ phase would be formed during cooling, and it would remain up to room temperature. The disappearance of the γ phase at 4 mass% of Si suggests that the fcc phase consists of Fe–Si alloys. Consequently, the added Si has uniformly dissolved into Fe, and Fe–Si alloys are synthesized in the present study.

3.3. Magnetic structure by Mössbauer spectrum analysis

The Mössbauer spectra of the samples S0–S4 are shown in Fig. 3. The results are summarized in Table 2. As mentioned in the previous section, the fcc γ-Fe phase represented by a singlet pattern near

Table 2
Mössbauer parameters of samples; δ: isomer shift, H_i: hyperfine field, Δ: quadrupole splitting, Γ: linewidth, and *A.R.*: calculated volume fraction.

		δ (mm/s)	H_i (T)	Δ (mm/s)	Γ (mm/s)	*A.R.* (%)
S0	A (γ-Fe)	−0.088	–	–	0.359	15.1
	B (α-Fe)	0.005	32.9	0.006	0.288	70.9
	C (Fe_3C)	0.219	20.8	0.061	0.465	14.0
S1	A (γ-Fe)	−0.084	–	–	0.317	11.1
	B (α-Fe)	0.006	33.0	0.003	0.300	68.1
	D (Fe–Si(I))	0.052	30.5	0.002	0.371	20.8
S2	A (γ-Fe)	−0.081	–	–	0.328	6.34
	B (α-Fe)	0.008	33.1	0.002	0.333	61.5
	D (Fe–Si(I))	0.057	30.6	0.011	0.386	29.8
	E(Fe–Si(II))	0.092	27.2	0.015	0.390	2.41
S3	A (γ-Fe)	−0.081	–	–	0.312	2.22
	B (α-Fe)	0.010	33.2	0.001	0.366	54.4
	D (Fe–Si(I))	0.058	30.7	0.016	0.393	38.6
	E(Fe–Si(II))	0.116	27.4	−0.007	0.300	4.86
S4	B (α-Fe)	0.012	33.2	−0.001	0.461	46.3
	D (Fe–Si(I))	0.055	30.8	0.016	0.461	41.1
	E(Fe–Si(II))	0.118	27.5	0.013	0.461	12.6

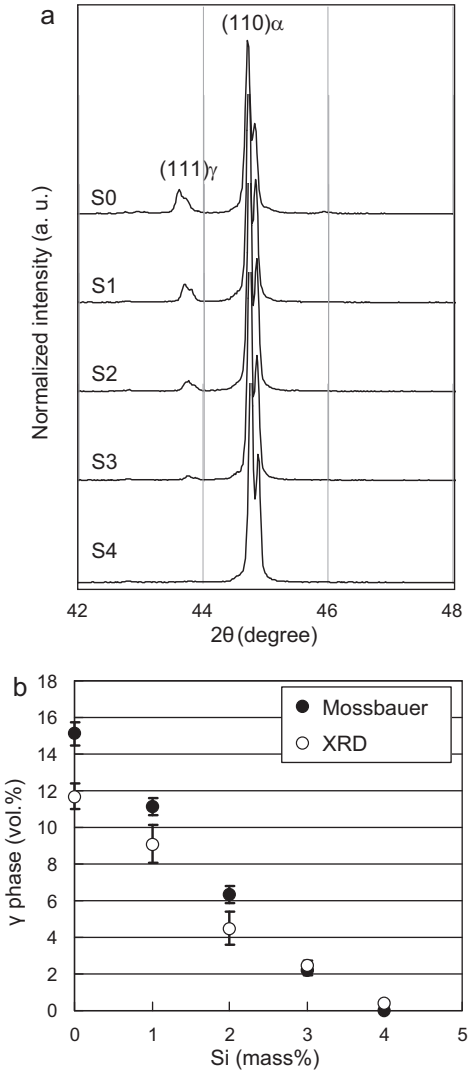

Fig. 2. Volume fractions of γ-Fe phase: (a) X-ray diffraction peaks, (b) estimated volume fraction of γ phase for each sample.

zero velocity (blue line in Fig. 3) decreases with the addition of Si, and disappears at 4 mass% of Si.

The sextets fitted by red line in Fig. 3 were assigned to the bcc α-Fe. They are the basic components in all samples. From the hyperfine fields "H_i," two types of the bcc phase, which are represented by "Fe–Si(I)" and "Fe–Si(II)" in Table 2, are assigned in the sample S1–S4. The Fe–Si(I) fitted by green line in Fig. 3 is the component that Si occupies as one of the nearest neighboring sites (8 sites) of an Fe atom in the bcc structure. The Fe–Si(II) fitted by pink line in Fig. 3 is one that Si atoms occupy two of the nearest neighbor-

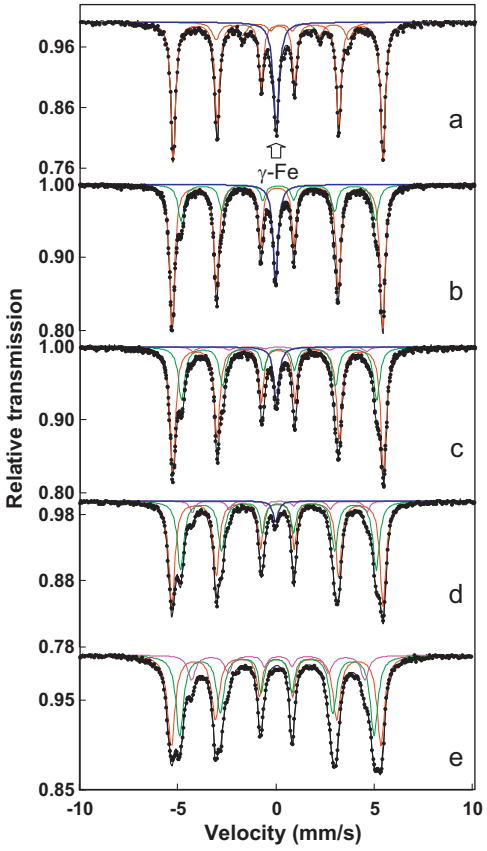

Fig. 3. Mössbauer spectrum of C-coated Fe particles with Si addition of (a) 0 mass% (S0), (b) 1 mass% (S1), (c) 2 mass% (S2), (d) 3 mass% (S3), and (e) 4 mass% (S4).

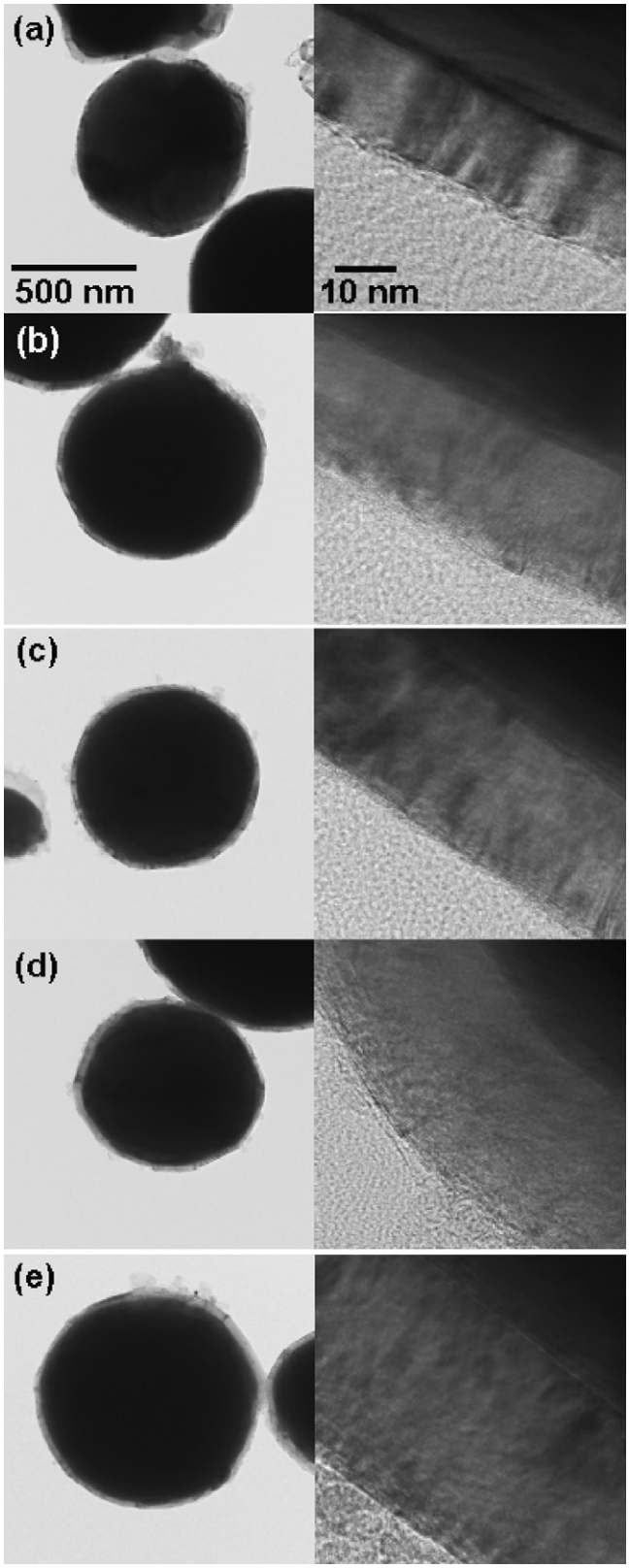

Fig. 4. Transmission electron micrographs of typical Fe particles and C coating layers. (a) S0, (b) S1, (c) S2, (d) S3, (e) S4.

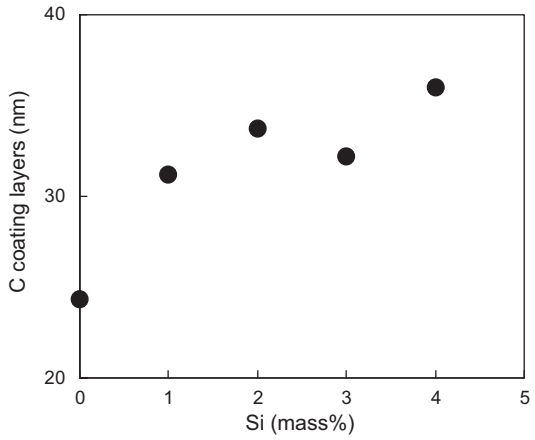

Fig. 5. Thickness of C coating layers as a function of Si addition.

ing sites of an Fe atom in the bcc structure. Each H_i of the Fe–Si(I) and Fe–Si(II) is 30.5–30.8 T and 27.2–27.5 T, respectively. The values are extremely similar to that of the reported one [21], which was 0.917 ± 0.005 and 0.834 ± 0.005 times the value of α-Fe. The calculated volume fractions ("*A.R.*" in Table 2) of Fe–Si(I) and Fe–Si(II) in the sample S2 are also similar to the calculated probability of each type of alloy in Fe–2.2mass%Si [21]. The appearance of these Fe–Si components suggests that Si dissolves in the bcc Fe phase.

Iron carbide (Fe_3C), which is fitted by brown line in Fig. 3(a), appears only in sample S0. The Fe_3C phase disappears by the addition of more than 1 mass% of Si. This means that Si easily alloys with Fe, and facilitates the decomposition of Fe–C.

3.4. Change in C coating layers in morphologies

Fig. 4 shows the TEM images of Fe particles encapsulated by C in samples S0–S4. The particle sizes of all samples are ~700 nm in diameter. The surface coating layers were assigned to graphitic C in the previous study [22]. The magnified images (right-side images) show that the C coating layers become thick as a result of the Si addition. The thickness of the C coating layers was measured for about 40 particles of each sample. The averaged thicknesses increase from 24 nm to 36 nm as shown in Fig. 5. It is considered that the addition of Si helps in precipitating C from the Fe cores, so that the graphitic C coating layers become thick.

Fig. 6 shows the backscattered electron images of samples S0 and S3. The surface coating of the sample S0 is inhomogeneous shown as the two-colored surface in Fig. 6(a). The white and gray area would represent bare Fe and C coating layers, respectively. Fig. 6(b) reveals that C coating layers encapsulate Fe homogeneously. The addition of Si is effective in creating thick coating layers and homogeneous coatings.

3.5. Corrosion resistance

In order to confirm homogeneous coatings, the corrosion resistance of samples S0–S4 was studied (Fig. 7). At first, Fe ion concentrations in the PBS buffer were measured after the soaking test, as shown in Fig. 7(a). The addition of Si clearly controls the elution of Fe ion to 1 ppm or less, which corresponds to10% or less of the Fe ion concentration eluted from the sample S0. Next, TG analysis was conducted as shown in Fig. 7(b). The samples were heated in air, and the weight changes were measured. In the TG curves, increase in the weight represents the oxidation of the samples. Carbonyl Fe powders as a reference begins to oxidize from 473 K. On the other hand, the oxidation beginning temperature is ~673 K and 800 K in samples S0 and S4, respectively. The samples

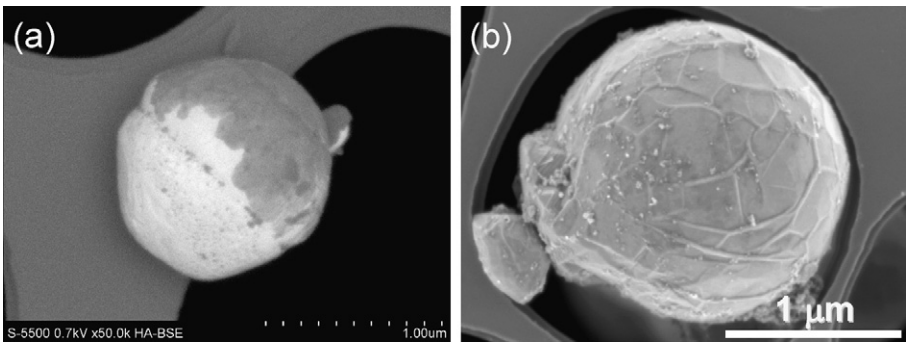

Fig. 6. Scanning electron microscopy images of C-coated Fe particles: (a) S0, (b) S3.

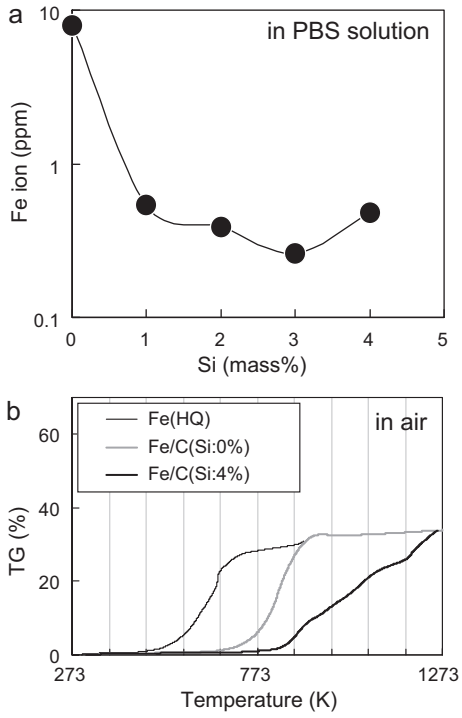

Fig. 7. Corrosion resistance of C-coated Fe particles. (a) Fe ion concentrations dissolved into PBS solution from S0–S4. (b) TG curves measured in air of S0 and S4 in comparison with commercial Fe particles.

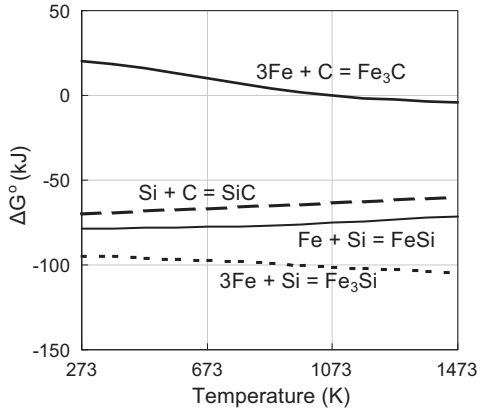

Fig. 8. Gibbs free energy for compounds of Fe_3C, SiC, FeSi and Fe_3Si.

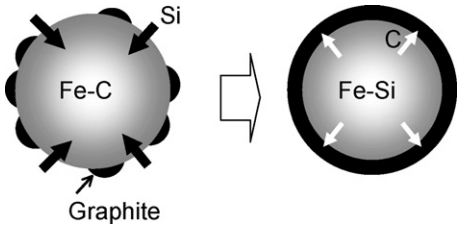

Fig. 9. Facilitated growth of C coating layers by the Si addition.

S0 and S4 exhibit excellent oxidation resistance, which is due to the C coating layers. Sample S4 has a highest oxidation beginning temperature. This suggests that Fe particles in S4 are sufficiently encapsulated with C.

3.6. Calculation of free energies

Gibbs free energies (ΔG) for each compound were calculated as shown in Fig. 8. The ΔG for FeSi and Fe_3Si is smaller than that of Fe_3C. This means that Fe alloys stably with Si and not C. Fig. 8 also shows that FeSi and Fe_3Si is stable compared with SiC. This suggests that the dissolution of Si in Fe is more stable than that in C. These results support that when the mixture of Fe, C, and Si is reacted, the formation of Fe–Si alloys is the most stable. As mentioned above, the addition of Si results in the decomposition of Fe_3C (Table 2) and the formation of sufficient C encapsulation (Figs. 4 and 6). The growth mechanism of the C coating layers is shown in Fig. 9. When Si is added into Fe–C particles, Si easily dissolves into Fe so that C leave the Fe cores to the surface, resulting in C coating layers.

4. Conclusion

Silicon carbide was added in the carbothermic reduction process, and the growth mechanism of the C coating layers on Fe particles was studied. Silicon successfully dissolved in Fe particles, so that the generation of Fe_3C was controlled. And then, the growth of the C coating layers was facilitated. Thermodynamic consideration suggests that Si helps in the decomposition of Fe–C. Therefore, the C coating layers result from the precipitation of C from Fe core particles. This supports the assumption that the growth of C coating layers on iron particles follow the "dissolution and precipitation model". Moreover, it is clear that the carbothermic reduction method in the present work can control the C coating layers by Si addition. This method is expected to contribute to industrialization of magnetic metal particles.

References

[1] K. Raj, R. Moskowitz, J. Magn. Magn. Mater. 85 (1990) 233–245.
[2] M.P. Sharrock, IEEE Trans. Magn. MAG-25 (1989) 4374–4389.
[3] M.E. Mchenry, S.A. Majetich, J.O. Artman, M. Degraef, S.W. Staley, Phys. Rev. B 49 (1994) 11358–11363.
[4] T. Gasche, M.S.S. Brooks, B. Johansson, Phys. Rev. B 53 (1996) 296–301.

[5] R. Semelka, T. Helmberger, Radiology 218 (2001) 27–38.
[6] R.S. Molday, D. Mackenzie, J. Immunol. Methods 52 (1982) 353–367.
[7] S. Goodwin, C. Peterson, C. Hoh, C. Bittner, J. Magn. Magn. Mater. 194 (1999) 132–139.
[8] R. Hiergeist, W. Andra, N. Buske, R. Hergt, I. Hilger, U. Richter, W. Kaiser, J. Magn. Magn. Mater. 201 (1999) 420–422.
[9] T. Hayashi, S. Hirono, M. Tomita, S. Umemura, Nature 381 (1996) 772–774.
[10] L. Díaz, M. Santos, C. Ballesteros, M. Maryško, J. Pola, J. Mater. Chem. 15 (2005) 4311–4317.
[11] Y. Saito, T. Yoshikawa, M. Okuda, N. Fujimoto, S. Yamamuro, K. Wakoh, K. Sumiyama, K. Suzuki, A. Kasuya, Y. Nishina, Chem. Phys. Lett. 212 (1993) 379–383.
[12] X.L. Dong, Z.D. Zhang, S.R. Jin, B.H. Kim, J. Appl. Phys. 86 (1999) 6701–6706.
[13] H. Tokoro, S. Fujii, T. Oku, J. Mater. Chem. 14 (2004) 253–257.
[14] B.C. Satishkumar, A. Govindaraj, R. Sen, C.N.R. Rao, Chem. Phys. Lett. 293 (1998) 47–52.
[15] H. Yan, Q. Li, J. Zhang, Z. Liu, Carbon 40 (2002) 2693–2698.
[16] A.A. Zhukov, V.I. Savulyak, T.F. Arkhipova, Met. Sci. Heat Treat. 42 (2000) 47–52.
[17] B.D. Cullity, Elements of X-ray Diffraction, 16th ed., Agune Syoufusya, Tokyo, 2004.
[18] G.F. Hanejko, W.G. Ellis, J.T. Hale, Advances in Powder Metallurgy & Particulate Materials, 2, 1998, 8.13-8.26.
[19] M. Polcarová, K. Godwod, J. Bak-misiuk, S. Kadečková, J. Brádler, Phys. Stat. Sol. (a) 106 (1998) 17–23.
[20] T.B. Massalski, J. Murray, L. Bennett, H. Baker, Binary Alloy Phase Diagrams, American Society for Metals, Ohio, 1986.
[21] M.B. Stearns, Phys. Rev. 129 (1963) 1136–1144.
[22] H. Tokoro, S. Fujii, S. Muto, S. Nasu, J. Appl. Phys. 99 (2006), 08Q512-1-3.